

Article

A Study on the Zener-Hollomon Parameter and Fracture Toughness of an Nb-Particles-Toughened TiAl-Nb Alloy

Jianbo Li ^{1,*}, Bin Liu ², Yan Wang ³, Shan Tang ⁴, Yong Liu ^{2,*} and Xiaofang Lu ¹

¹ School of Materials Science and Engineering, Chongqing University, Chongqing 400044, China; 20160913160@cqu.edu.cn

² State Key Laboratory of Powder Metallurgy, Central South University, Changsha 410083, China; binliu@csu.edu.cn

³ School of Aeronautics and Astronautics, Central South University, Changsha 410083, China; wangyan@csu.edu.cn

⁴ State Key Laboratory of Structural Analysis for Industrial Equipment, Department of Engineering Mechanics, Dalian University of Technology, Dalian 116023, China; shan_tang_0917@163.com

* Correspondence: lijianbo1202@cqu.edu.cn (J.L.); yonliu@csu.edu.cn (Y.L.); Tel.: +86-23-6510-2060 (J.L.); +86-731-8883-0406 (Y.L.)

Received: 20 March 2018; Accepted: 19 April 2018; Published: 21 April 2018



Abstract: Hot compressive deformation behaviors of a powder metallurgy Ti-45Al-5Nb-0.4W/2Nb (at. %) were investigated at strain rates from 0.001 s^{-1} to 1 s^{-1} and temperatures from $1050\text{ }^{\circ}\text{C}$ to $1200\text{ }^{\circ}\text{C}$. The Zener-Hollomon (Z) parameter can affect the hot deformation mechanism significantly. At a high Z condition, Nb particles played an important role in coordinating the deformation. At a low Z condition, deformation of Nb particles accompanied by dynamic recrystallization (DRX) can act as a dominant softening mechanism. The as-forged pancake exhibits a short rod-like particle-toughened equiaxed matrix. For notched three-point bending (3PB) tests, the fracture toughness of an Nb-particles-toughened high-Nb-containing duplex phase γ -TiAl alloy was hardly affected by the loading rate, presenting a peak fracture toughness of about $12.9\text{ MPa}\cdot\text{m}^{1/2}$. The toughness of the present alloy can be improved by ductile Nb particles. A model based on the Griffith-Orowan-Irwin relation was constructed, which is quite accurate to predict the fracture toughness of the present specimen using tensile properties.

Keywords: TiAl alloy; Zener-Hollomon parameter; Nb particle; fracture toughness

1. Introduction

TiAl-based alloys are currently of considerable interest as advanced high-temperature structural materials owing to their low density, good elevated-temperature strength, and high oxidation resistance [1–3]. Recently, many kinds of Nb in the order of 5–10% have been used to develop new kinds of TiAl alloys, such as Ti-45Al-(5–10)Nb alloys. In these alloys, Nb plays an important role in enhancing high-temperature strength and antioxidation ability [4–7]. However, the application of monolithic high-Nb-containing γ -TiAl alloy is limited due to its relatively poor fracture toughness.

Recent studies have shown that in situ TiAl matrix composites reinforced with homogeneously distributed ceramic particles have higher fracture toughness due to their smaller reinforcement size and clean reinforcement-matrix interface [8–10]. Unfortunately, large particle clusters containing large amounts of small particles would appear in the matrix, and these clusters were detrimental to the plastic deformation due to their sudden breaking apart [11]; additionally, cracking along precipitates would lead to poor performance [12]. Therefore, it seems that sometimes the fracture toughness cannot

be improved by ceramic particles. It has been reported that an improvement in the fracture resistance of a brittle intermetallic can be achieved by adding ductile phase [13–15]. The increase in toughness is mainly associated with unbroken ductile ligaments in the bridging zone and the subsequent crack bridging via plastic stretching of these ligaments. A loss of local constraint around particles and crack deflection can further contribute to toughening. Yang et al. [16] has found that ductile Nb phase can absorb the fracture energy in front of the cracks and that the propagation of the cracks can be branched by B2 phase in a TiAl-Nb composite. Chen et al. [17] has found that precipitation of lots of fine γ and β particles from α lamellae can result in a large number of γ/α_2 and β/α_2 interfaces, which retards dislocation motion in a bending test, and thus leads to a higher K_{IC} (23.5 MPa·m^{1/2}) at room temperature for a β -phase-containing TiAl alloy. Rao [18] found that for TiNb- and Nb-toughened composites, toughness increases with increasing reinforcement thickness, ductile content, and strength.

The most attention has been paid to the fracture mechanism of TiAl composites with an FL (full lamellar) microstructure. The fracture toughness of TiAl composites with FL is higher than that of TiAl composites with a duplex (DP) microstructure, but a high-Nb-containing TiAl alloy with a duplex microstructure has better comprehensive mechanical performance [2]. However, the crack growth response of a ductile-particle-toughened, high-Nb-containing duplex phase γ -TiAl alloy has been largely overlooked, and there is little literature on prediction models of K_{IC} for ductile Nb-particles-toughened γ -TiAl alloys. It is believed that grain refinement by hot working is a very effective approach to enhance the overall performance of γ -TiAl alloys, yet the hot-working behaviors of a ductile-particle-toughened, high-Nb-containing duplex phase γ -TiAl alloy have not been fully reported, and studies on the relationship between the Zener-Holloman parameter and the deformation mechanism are still limited.

The objective of this paper is to investigate the hot deformation mechanisms of a Nb-particles-toughened, high-Nb-containing PM-TiAl alloy at various Zener-Holloman (Z) parameters and the fracture toughness of a ductile Nb-particles-toughened, high-Nb-containing duplex phase γ -TiAl alloy, which can help us to understand the fracture mechanism of the TiAl composite.

2. Experimental

An as-cast Ti-45Al-5Nb-0.4W ingot with a dimension of $\varphi 75$ mm \times 400 mm was used in plasma rotating electrode processing (PREP) as an electrode material, then rotated at a speed of 16,000 r/min and atomized. The pre-alloyed powder was screened, and the mean particle size was found to be about 80 μ m. The mean size of the Nb elemental powder was about 100 μ m. The two kinds of powder were mixed for about 4 h with a weight ratio of TiAl:Nb = 95.6:4.4. The powder metallurgy (PM) technique has been adopted to synthesize a PM-TiAl alloy with a nominal composition of Ti-45Al-5Nb-0.4W (at. %) and Nb elemental powder (2 at. %).

The mixed powder was filled into a stainless-steel can with a size of 450 mm \times 400 mm \times 120 mm. Then, the can was sealed and degassed at 500 °C for 12 h. A hot isostatic pressing (HIP) process was conducted at a temperature of 1250 °C and a pressure of 170 MPa for 5 h. A TiAl alloy pancake was obtained after removing the can.

The specimens for compression were cut by electric-discharge machining with a height of 12 mm and a diameter of 8 mm, and the compression tests were conducted at strain rates from 0.001 s⁻¹ to 1 s⁻¹, and temperatures from 1050 °C to 1200 °C, using a thermecmastor-Z thermal simulator (Fuji Electric Machinery Co., Ltd., Tokyo, Japan). The samples were heated at rate of 5 °C/s and homogenized for 5 min at the target temperature. The maximum nominal deformation was 60%. Finally, the samples were quenched in water to preserve the deformed microstructure. Protective lubricant and graphite paper glass were used to reduce the friction.

A cylindrical billet ($\varphi 50$ mm \times 80 mm) was cut from the HIP block and degassed in 1.5-mm-thick cans made by special steel, then canned forged at 1200 °C with an engineering strain of 80%. The outer pack can offset the secondary stress generated in the forging process and avoid cracks in billets. Finally, heat treatment was performed at 1260 °C for 2 h followed by air cooling.

The specimens for the scanning electron microscopy (SEM, JSM-6360, JEOL, Tokyo, Japan) and optical metallographic observations were mechanically polished and then etched in Kroll's reagent. For transmission electron microscopy (TEM, JEOL-2100F, JEOL, Tokyo, Japan) observation, the specimens were first mechanically ground to a thickness of 70 μm and then thinned by a twin-jet polishing machine (Struers, Ballerup, Denmark) in a solution of 50% methanol, 29% *n*-butyl alcohol, and 21% perchloric acid with the voltage at 22.5 V and at a temperature of $-30\text{ }^{\circ}\text{C}$. The TEM observation was conducted on a transmission electron microscope (JEOL-2100F) with the voltage at 200 kV.

Tensile samples were cut by electric-discharge machining from the centre of the deformed pancake. The gauge section of the cross-section was 3 mm \times 1.2 mm and the length was 8 mm. The tensile tests were undertaken at room temperature with a strain rate of $2.0 \times 10^{-4}\text{ s}^{-1}$ on an Instron 1341 test machine (Instron, Norwood, MA, USA).

The single-edge, notched-bend specimens were prepared referring to the ASTM E399-17 standard. The dimensions of the specimens for notch three-point bending (3PB) tests are shown in Figure 1. The slit notch was cut by an electro-discharge machine with a width of 170 μm . The specimens were polished by SiO_2 paper before testing. Notch three-point bending (3PB) tests were conducted by the INSTRON 1341 test machine at room temperature, with cross-head rates of 0.05 and 0.5 mm/min.

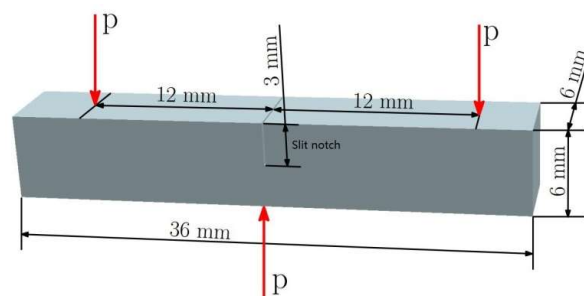


Figure 1. Shapes and dimensions of bending specimen (mm).

3. Results

3.1. Starting Microstructure

The starting material is mainly composed of two parts as shown in Figure 2: a matrix material (dark region) and white spheroidal particles distributed in the matrix randomly. Combining them in the Ti-Al-Nb system [19], it can be determined that the Nb particles are primarily composed of β (B2), ω phase, and pure Nb in the center, and the matrix is mainly composed of γ and α_2 phase as shown by the arrow. For detailed information, the reader is referred to our previous work [20].

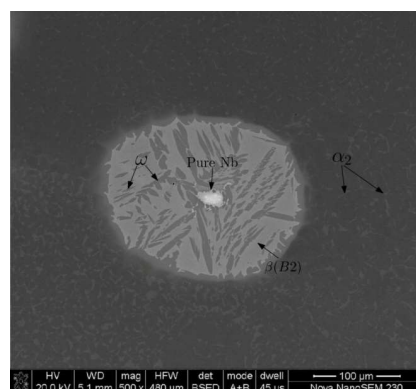


Figure 2. Microstructure of the Ti-45Al-5Nb-0.4W/2Nb (at. %) alloy before compression.

3.2. Deformation Behavior

Figure 3 shows the flow curves of the Ti-45Al-5Nb-0.4W/2Nb (at. %) alloys compressed at different strain rates and temperatures. It can be found that the flow stress is related to the strain rate and the deformation temperature. With a decreasing strain rate and an increasing temperature, the flow stress decreases obviously. At the initial hot deformation stage, most of the curves present a single stress; after the peak point, they drop until they reach a steady state with the strain increasing.

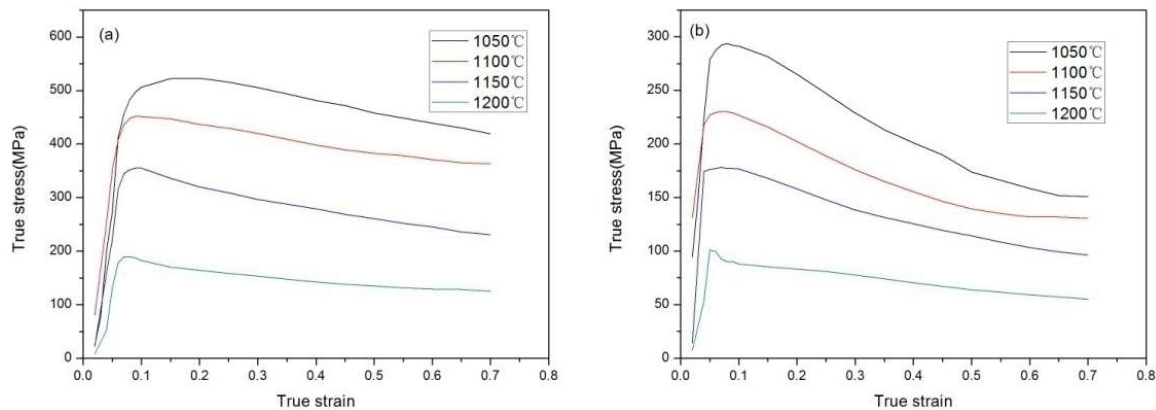


Figure 3. Flow curves of the Ti-45Al-5Nb-0.4W/2Nb (at. %) alloy at: (a) 1 s^{-1} and different temperatures; (b) 0.01 s^{-1} and different temperatures.

A constitutive equation is proposed by Sellars et al. [21] to describe the relationship between the deformation parameters and the flow stress. The flow behavior of alloys during hot deformation can be considered as a thermally activated process, which can be expressed as:

$$Z = \dot{\varepsilon} \exp\left(\frac{Q}{RT}\right) = A[\sinh(\alpha\sigma)]^n \quad (1)$$

where Z is the Zener–Hollomon parameter, $\dot{\varepsilon}$ is the deformation strain rate, Q is the apparent activation energy during deformation (kJ/mol), R is the molar gas constant (8.314 J/mol·K), σ is the flow stress, T is the deformation temperature (K), and A , α , and n represent material constants as shown in Figure 4. The activation energy (Q) value can be obtained by a transformation from Equation (1):

$$Q = R \left\{ \frac{\partial \ln \dot{\varepsilon}}{\partial \ln[\sinh(\alpha\sigma)]} \right\}_T \cdot \left\{ \frac{\partial \ln[\sinh(\alpha\sigma)]}{\partial (1/T)} \right\}_{\dot{\varepsilon}} \quad (2)$$

The relationships of $\ln \dot{\varepsilon}$ versus $\ln[\sinh(\alpha\sigma)]$ and $\ln[\sinh(\alpha\sigma)]$ versus $1/T$ can be obtained on the basis of Equation (2). Therefore, for the Ti-45Al-5Nb-0.4W/2Nb (at. %) alloy, the activation energy calculated at different true strains can be achieved as shown in Figure 4d.

The relationship between the Zener-Hollomon parameter (Z) and the deformation condition is shown in Figure 5. The Zener-Hollomon parameters were obtained on the basis of Equation (1). The Zener-Hollomon parameter decreases with a decreasing strain rate and an increasing temperature. The map can be divided into two domains: a high Z domain ($\ln Z \geq 35.0$) and a low Z domain ($\ln Z < 35.0$).

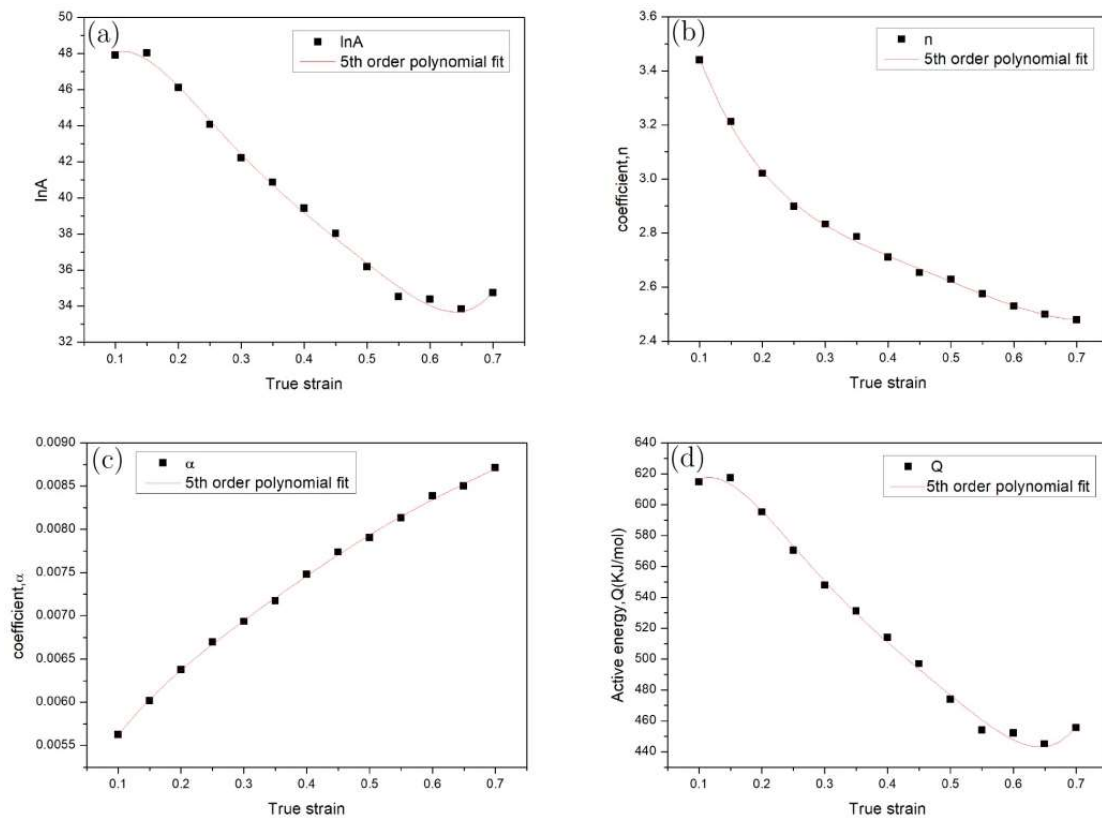


Figure 4. Plots used for calculation of: (a) A , (b) n , (c) α , and (d) deformation activation energy.

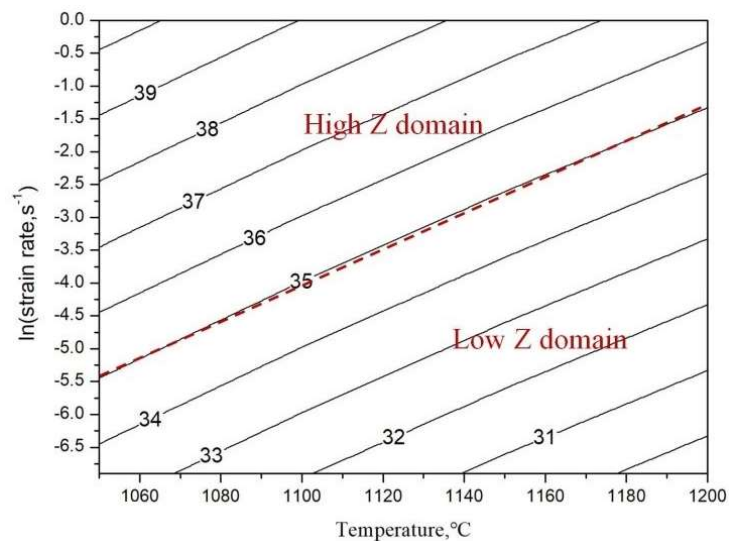


Figure 5. Zener-Hollomon parameter ($\ln Z$) of the Ti-45Al-5Nb-0.4W/2Nb (at. %) alloy at different temperatures and strain rates (the numbers on the contour lines are the values of $\ln Z$).

Figure 6 shows the SEM microstructures of samples deformed at different strain rates and deformation temperatures. It can be clearly seen that at $\ln Z = 40.44$ (high Z, $1050^{\circ}\text{C}/1\text{ s}^{-1}$), many cracks appear at the edge of the deformed specimen, which are shown in Figure 6a,b, and the crack propagates either through the Nb particles or along the interface of the Nb particles.

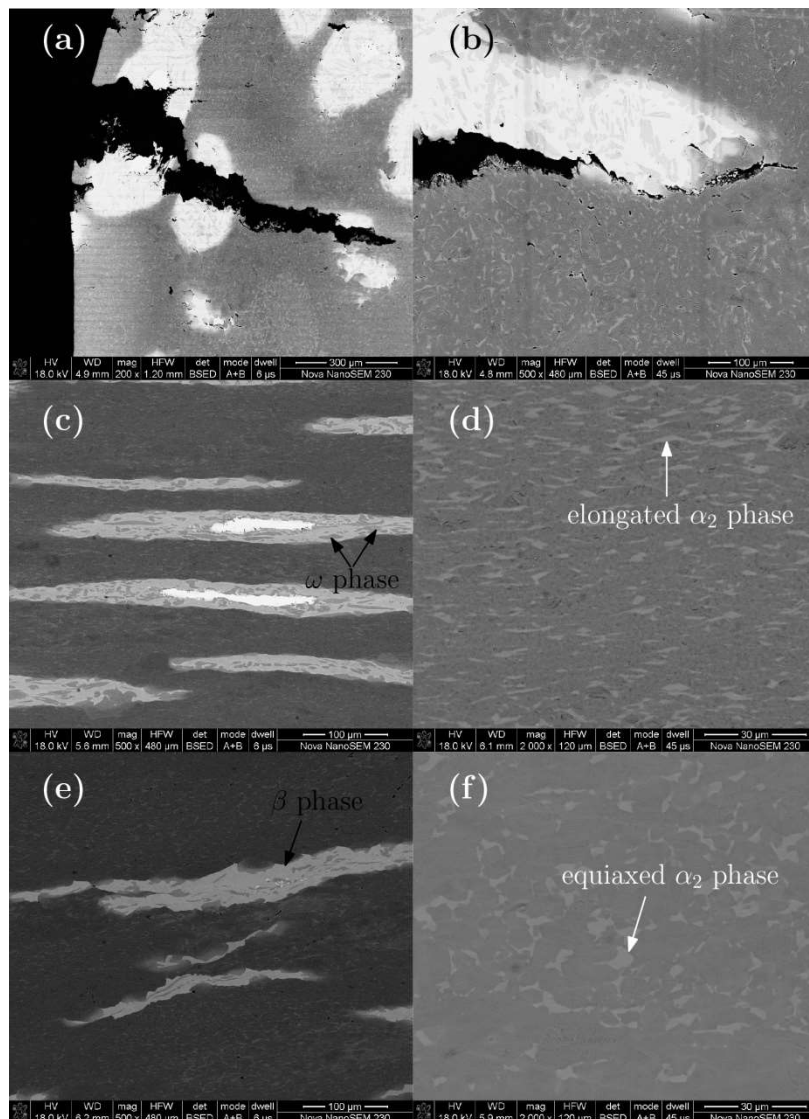


Figure 6. BSE (backscattered electron) micrographs of the Ti-45Al-5Nb-0.4W/2Nb (at. %) alloy deformed to a true strain of 0.7 at different Z values: (a–d) $\ln Z = 40.44$ (high Z , $1050\text{ }^{\circ}\text{C}/1\text{ s}^{-1}$); (a,b) show cracks appearing at the edge of the specimen; (c) shows the elongated Nb particles and part of the residual pure Nb in the center; (d) shows the elongated α_2 grains in the matrix; (e,f) $\ln Z = 30.70$ (low Z , $1150\text{ }^{\circ}\text{C}/0.001\text{ s}^{-1}$); (e) shows the serration boundary of elongated Nb particles; (f) shows the equiaxed α_2 grains in the matrix.

At the middle of the deformed specimen, the spheroidal Nb particles were deformed into short rods as shown in Figure 6c, and the α_2 grains were elongated or even broken up (Figure 6d). As the Z value decreases, the boundary of elongated Nb particles presents serration indicating diffusion of Nb element, the proportion of β (B2) phase in the Nb particles increases while the proportion of ω phase decreases (Figure 6e), and the α_2 grains presented an equiaxed shape, indicating that dynamic recrystallization may happen (Figure 6f).

The bright-field TEM images of the deformed microstructures are shown in Figure 7. At a high Z value, a high density of dislocations can be observed in the γ grains (Figure 7a). The residual lamellar colony is bent, and deformation twins, which form bundles, are observed in the γ lamella as shown in Figure 7b. Generally, the recrystallization process begins with recovery and the rearrangement of

dislocations is beneficial to form a low-energy configuration. When the Z value is sufficiently low, fine dislocation-free recrystallized γ grain can be clearly seen as in Figure 7c.

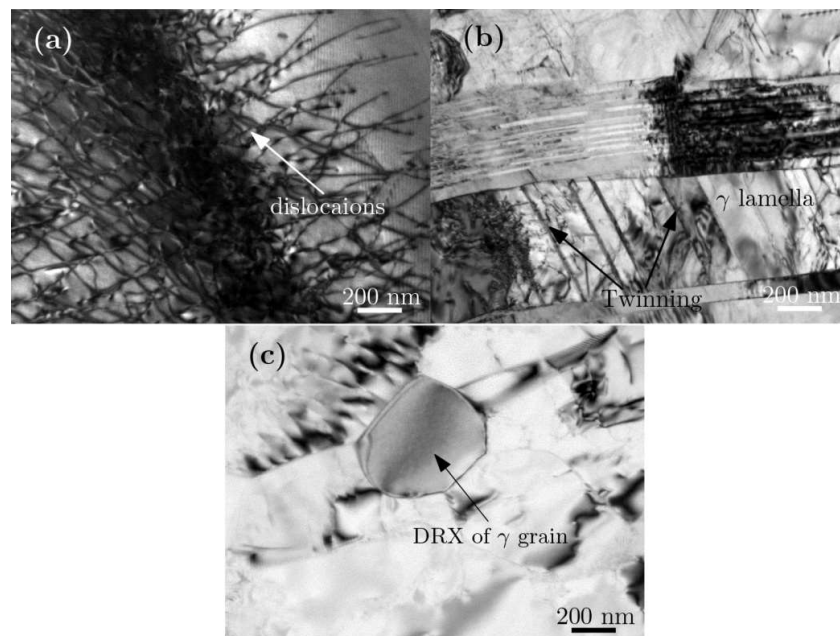


Figure 7. TEM images of Ti-45Al-5Nb-0.4W/2Nb (at. %) deformed to a true strain of 0.7 at different Z values: (a,b) $\ln Z = 40.44$ (high Z , $1050\text{ }^\circ\text{C}/1\text{ s}^{-1}$); (a) shows the high density of dislocations in γ grains; (b) shows the residual lamellar colony with the dislocations and twins; (c) shows the recrystallized γ grain at $\ln Z = 30.70$ (low Z , $1150\text{ }^\circ\text{C}/0.001\text{ s}^{-1}$).

In actual industrial production, to avoid the occurrence of cracks, low Z conditions (lower strain rates and higher temperatures) are usually preferred; however, when the deformation rate is too low, the temperature drop is serious, which is harmful for deformation [22]. Therefore, hot forging of a cylindrical billet ($\varphi 50\text{ mm} \times 80\text{ mm}$) was conducted at a lower Z condition but with a higher deformation rate ($\ln Z = 34.02$, $1200\text{ }^\circ\text{C}/0.1\text{ s}^{-1}$), and a forged pancake was achieved, as shown in Figure 8a, in which cracks can be hardly detected. Then, the pancake was heated at $1260\text{ }^\circ\text{C}$ for 2 h followed by air cooling. The deformed microstructure at the core area of the pancake is shown in Figure 8b, which is mainly composed of the matrix with a duplex phase microstructure and white short rod-like Nb particles distributed in the matrix randomly.

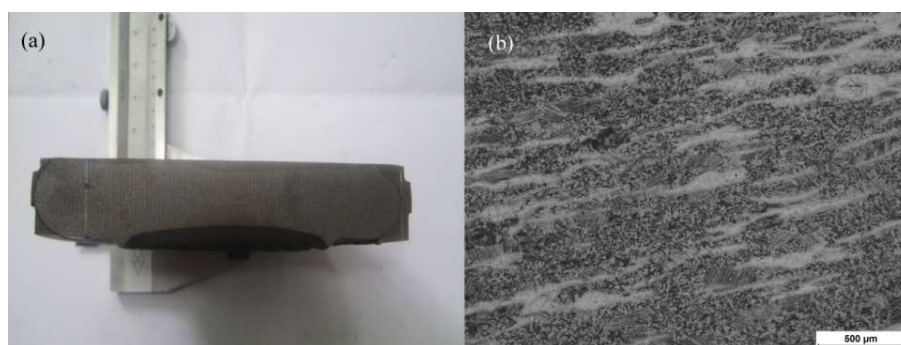


Figure 8. Hot pack forging of a Ti-45Al-5Nb-0.4W/2Nb (at. %) alloy billet: (a) the cross-section of the deformed billet; (b) the optical metallographic microstructure in the center of the billet after heat treatment of $1260\text{ }^\circ\text{C}/2\text{ h}$ with air cooling.

3.3. Tensile Tests

The tensile properties of the as-forged Ti-45Al-5Nb-0.4W/2Nb (at. %) alloy were tested at a speed of $2 \times 10^{-4} \text{ s}^{-1}$. The average ultimate tensile strength (UTS) was 342 MPa, and with an elongation of 1.2%, the alloy presents brittle fracture. Compared with Figure 9a,b, the fracture surface where Nb particles are located can be found, the fracture surface is relatively smooth, indicating that transgranular cleavage fracture occurred, and the Nb particles can be pulled out due to their weak interfacial adhesion. Some cracks are found inside the Nb particles, or along the boundary, as shown by arrows in Figure 9a.

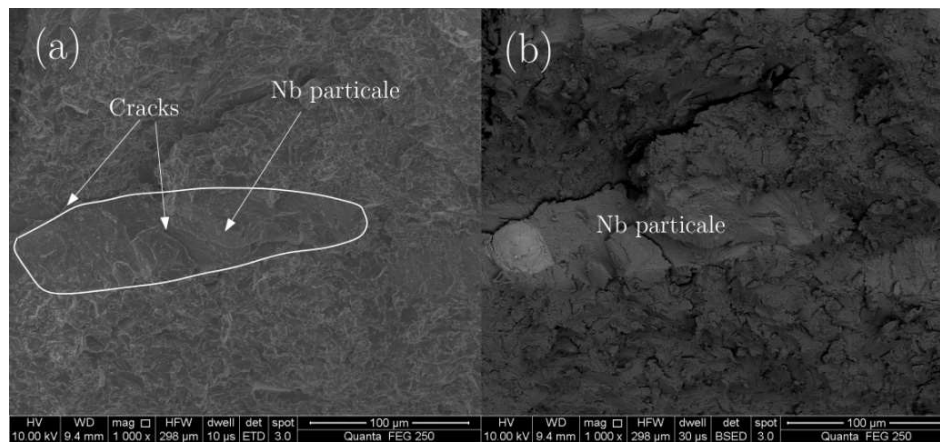


Figure 9. Fracture surface of tensile specimen tested at room temperature: (a) shows the region initiating the fracture in the secondary-electron emission model; (b) shows the BSE fracture corresponding to (a).

3.4. Bending Tests

The fracture load (P) was obtained from the load-displacement flow curve, and the energy (w) in the fracture was calculated by the area under the flow curve. The values of K_{IC} (notch) were calculated by the following equation [23,24]

$$S = 4W \quad (3)$$

$$K_{IC} = \left(\frac{SP_q}{BW^{3/2}} \right) Y_{(a/w)} \quad (4)$$

$$Y_{(a/w)} = \left[\frac{3(a/w)^{1/2} \left\{ 1.99 - (a/w)(1 - a/w) \left[2.15 - 3.93(a/w) + 2.7(a/w)^2 \right] \right\}}{2(1 + 2a/w)(1 - 2a/w)^{3/2}} \right] \quad (5)$$

Here, K_{IC} (notch) is the stress intensity factor for notched specimen; S is the span of loading; W and B are the width and thickness of specimen, respectively; and a is the length of the slit notch. P_q is measured by the load-displacement flow curve according to the standard of GB/T 4161-1984.

The fracture toughness of TiAl alloys with a duplex microstructure is shown in Table 1. It can be found that the average fracture toughness (K_{IC}) of a TiAl alloy with a duplex microstructure can reach $12.9 \text{ MPa}\cdot\text{m}^{1/2}$ when the loading rate is 0.5 mm/min ; however, the fracture toughness is almost not affected by the loading rate.

Table 1. Three-point bending (3PB) test results for the TiAl alloy with a duplex (DP) microstructure in displacement-controlled mode.

V (mm/min)	P_{\max} (N)	K_{IC} (MPa·m ^{1/2})
0.05	550	12.65
0.5	561	12.90

The cross-sectional crack path from the centre of samples that were unloaded before final fracture is shown in Figure 10. It can be found that the path of crack propagation is mainly transgranular and the linearity is obvious. When a crack arrived at an Nb particle, it was divided into two cracks; thus, crack branching occurred and the crack was finally arrested at the boundary of the Nb particle as shown by the arrow in Figure 10. The fracture surface of the 3PB test specimen is shown in Figure 11. It exhibits a mixture of the features of fine inter- and translamellar cracks, which accords with the side-view images from Figure 10, and crack deflection can be found when the crack reaches the Nb particle as shown by the arrow.

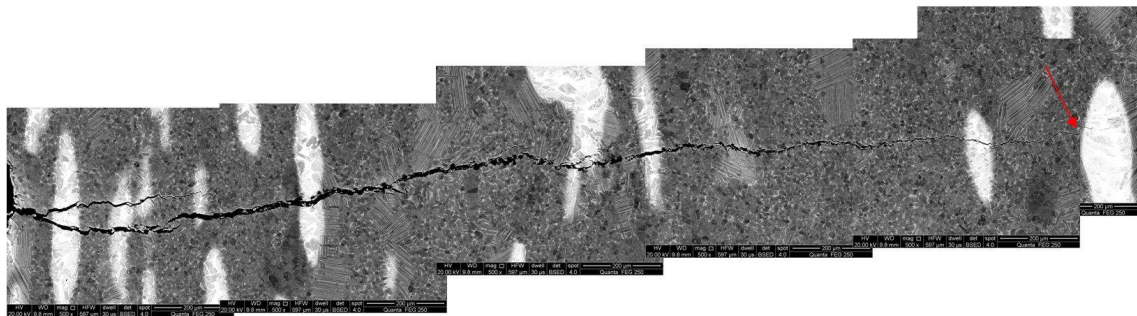


Figure 10. Crack path of the Ti-45Al-5Nb-0.4W/2Nb (at. %) alloy with a DP microstructure tested at room temperature with a loading rate of 0.05 mm/min.

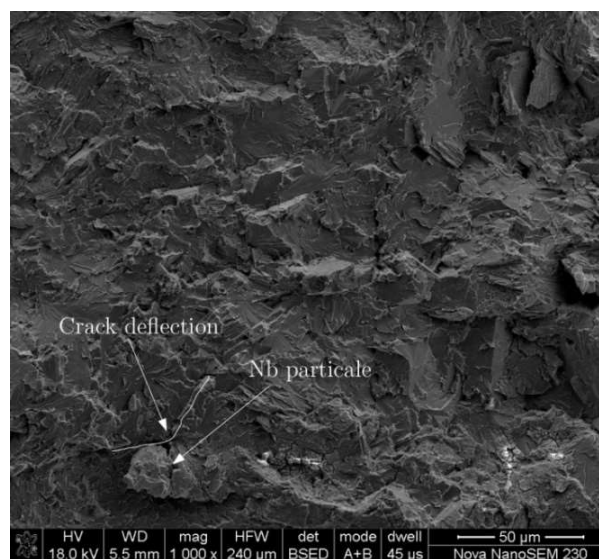


Figure 11. The fracture surface of the 3PB Ti-45Al-5Nb-0.4W/2Nb (at. %) alloy with a DP microstructure tested at room temperature with a loading rate of 0.05 mm/min.

4. Discussions

4.1. Effect of Zener-Holloman Parameter on Hot Deformation Mechanism

It is found that the hot deformation behavior of the Ti-45Al-5Nb-0.4W/2Nb (at. %) alloy is closely related to the combined effects of the deformation temperature and the strain rate, which can be expressed by the Zener-Hollomon parameter (Z) [25] as shown in Figure 5. At a high Z condition, the Nb particles contained a large amount of β phase, and the β phase was expected to be softer during hot deformation due to its disordered lattice [26]. Additionally, there were more independent slip systems in the β phase than there were in the matrix (α_2 phase and γ phase);

thus, Nb particles played an important role in coordinating the deformation. However, due to the high tensile stress at the edge of deformed specimens, cracks can be easily found inside Nb particles or along the interface of the Nb particles. The plastic deformation of γ -TiAl alloy takes place by dislocation slip and mechanical twinning. Generally, slip proceeds by four common unit dislocations of $1/2\langle 110 \rangle \{111\}$, eight superlattice dislocations of $\langle 101 \rangle \{111\}$, and four twinning systems $1/6\langle 11\bar{2} \rangle \{111\}$ [27]. At a high Z condition, dislocation accumulation can easily occur in the γ grains; however, in the lamellar structures, the dislocation mobility decreases and twinning in γ lamella can provide an alternative deformation mechanism in order to accommodate large strain (Figure 7b). This is due to the fact that twinning partial dislocations were activated by interfacial dislocations in the lamellar microstructure [28,29]. The breakup of α_2 grains can also coordinate the deformation at a high Z condition. The low Z condition is beneficial for the diffusion of Nb element; as a result, the decrease of ω content in the Nb particles can contribute to softening. This is due to the fact that fine ω precipitates are responsible for the higher strength of the β phase, and these precipitates also decrease the ductility of the β phase by hindering dislocation slip [30]. The flow softening of the matrix at a low Z condition is mainly attributed to the appearance of dynamic recrystallization (DRX). The fine DRX γ grains and α_2 grains in the microstructure can promote the movement and rotation of the grain boundary during deformation and contribute to the improvement of hot deformability.

4.2. Effect of Nb Particles on Fracture Toughness Mechanism

As there are limited reports on the fracture toughness of TiAl-Nb alloys with a duplex microstructure, we cannot find out enough data to make a comparison, but the results we obtained are summarized in Table 2. It can be found that the toughness of a TiAl alloy with a duplex microstructure can be improved by reinforcing it with ductile Nb particles. There are two reasons for the higher K_{IC} . Firstly, the TiAl alloy with a duplex microstructure exhibits little plastic strain close to the onset of crack extension and nearly no resistance to crack propagation [31]; however, for the present alloy, Nb particles containing a large amount of β (B2) phase can retard crack propagation due to the lower hardness of the β (B2) phase [32]. Secondly, crack branching and crack deflection may occur when a crack reaches Nb particles. As shown in Figures 10 and 11, the energy of the main crack's propagation can be reduced effectively.

Table 2. The peak fracture toughness of high Nb-TiAl alloy with a duplex microstructure.

Alloys	Microstructure	K_{IC} (MPa·m ^{1/2})
Ti-45Al-5Nb-0.4W/2Nb (at. %) [this work]	DP	12.9
Ti-46.5Al-5.3Nb (at. %) [33]	DP	9
Ti-45Al-5Nb-4C-0.2B (at.%) [34]	DP	11

4.3. Prediction of K_{IC}

The capacity of an alloy to resist crack propagation can be determined by the critical energy consuming rate G_{IC} under plane strain conditions. The relation between G_{IC} and the critical stress intensity factor K_{IC} is shown as Equation (6) [33]

$$K_{IC} = \sqrt{\frac{G_{IC}E}{(1-\nu^2)}} \quad (6)$$

where E and ν are Young's modulus and Poisson's ratio, respectively. Based on the Griffith-Orowan-Irwin relation [34], G_{IC} can be written as

$$G_{IC} = 2(\gamma_s + \gamma_p) = 2\gamma_{eff} \quad (7)$$

where γ_s is the surface energy per unit at the crack tip which is to produce unstable crack propagation, γ_p is the crack surface's energy consumed in plastic deformation, and γ_{eff} is the effective surface energy. The relation between the effective surface energy γ_{eff} and the work of deformation in tension A_e is shown as

$$2\gamma_{\text{eff}} = 0.8lA_e \quad (8)$$

where l is a characteristic constant of length, whose size is close to that of the critical crack in the plane strain condition. The value of l can be obtained by Equation (9).

$$l = 0.25(K_{IC}/UTS)^2 \quad (9)$$

According to the report by Zheng [35], A_e can be written as

$$A_e = \int_0^{\varepsilon_u} \sigma d\varepsilon \approx \frac{(EL_u - \frac{YS}{E})(YS + 2UTS)}{3} + \frac{YS^2}{2E} \quad (10)$$

where σ is the flow stress during a tensile test, YS is the yield stress, and ε_u and EL_u are the uniform strain and the uniform deformation elongation, respectively. As Nb particles toughen the PM γ -TiAl alloy and prevent brittle fracture, the tensile stress has no yield point. Therefore, YS can be replaced by UTS . Equation (10) can be changed into:

$$A_e = \left(EL_u - \frac{UTS}{E}\right)(UTS) + \frac{UTS^2}{2E} \quad (11)$$

Thus, K_{IC} can be determined as follows:

$$K_{IC} = \sqrt{\frac{0.8lE}{(1-\nu^2)} \cdot \left(EL_u \cdot UTS - \frac{UTS^2}{E}\right)} \quad (12)$$

To predict the fracture toughness K_{IC} by Equation (12), the Young's modulus of Ti-22Al-24Nb (134 GPa [36]) is taken as the E of Ti-45Al-5Nb-0.4W/2Nb (at. %) approximately in this paper. The value of l for DP microstructures is 3.5×10^{-4} m. The Poisson's ratio is 0.35 [35]. The predicted fracture toughness of DP microstructures is $12.44 \text{ MPa}\cdot\text{m}^{1/2}$. Compared to the experimentally tested peak fracture toughness, the error is just $0.46 \text{ MPa}\cdot\text{m}^{1/2}$. This indicates that the model (Equation (12)) can predict the fracture toughness of the Ti-45Al-5Nb-0.4W/2Nb (at. %) alloy accurately.

5. Conclusions

- (1) The Zener-Hollomon parameter can affect the hot deformation mechanism significantly. At a high Z condition, Nb particles played an important role in coordinating the deformation. At a low Z condition, deformation of Nb particles accompanied by dynamic recrystallization (DRX) became the dominant softening mechanism.
- (2) For the notched 3PB-tested Nb-particles-toughened high-Nb-containing γ -TiAl alloy with DP specimen, the fracture toughness was almost not affected by the loading rate, with a peak fracture toughness of about $12.9 \text{ MPa}\cdot\text{m}^{1/2}$.
- (3) The toughness of the TiAl alloy with a duplex microstructure can be improved by reinforcing it with ductile Nb particles. Nb particles can retard crack propagation and crack branching and crack deflection can further contribute to toughening.
- (4) The fracture toughness prediction model based on the Griffith-Orowan-Irwin relation is quite suitable for predicting the fracture toughness of the Nb-particles-toughened DP specimen using tensile properties.

Acknowledgments: The authors would like to thank the National Natural Science Foundation of China (51601022 and 51301204), the fundamental research funds for the central universities of China (106112016CDJXY130007), and the Hunan Natural Science Foundation of China (2017JJ2311) for the financial support.

Author Contributions: Jianbo Li and Yong Liu conceived and designed the experiments; Bin Liu, Yan Wang, and Shan Tang analyzed the data; Jianbo Li and Xiaofang Lu performed the experiments and collected the data; Jianbo Li wrote the paper.

Conflicts of Interest: The authors declare no conflict of interest.

References

1. Clemens, H.; Mayer, S. Design, processing, microstructure, and applications of advanced intermetallic TiAl alloys. *Adv. Eng. Mater.* **2013**, *15*, 191–215. [[CrossRef](#)]
2. Kunal, K.; Ramachandran, R.; Norman, M.W. Advances in gamma titanium aluminides and their manufacturing techniques. *Prog. Mater. Sci.* **2012**, *55*, 1–16.
3. Liss, K.D.; Funakoshi, K.I.; Dippenaar, R.J.; Higo, Y.; Shiro, A.; Reid, M.; Suzuki, H.; Shobu, T.; Akita, K. Hydrostatic compression behavior and high-pressure stabilized β -phase in γ -based titanium aluminide intermetallics. *Metals* **2016**, *6*, 165. [[CrossRef](#)]
4. Xiang, L.; Tang, B.; Xue, X.Y.; Kou, H.C.; Li, J.S. Characteristics of the dynamic recrystallization behavior of Ti-45Al-8.5Nb-0.2W-0.2B-0.3Y alloy during high temperature deformation. *Metals* **2017**, *7*, 261. [[CrossRef](#)]
5. Ding, J.; Lin, J.P.; Zhang, M.H.; Dong, C.L.; Liang, Y.F. High-temperature torsion induced gradient microstructures in high Nb-TiAl alloy. *Mater. Lett.* **2017**, *209*, 193–196. [[CrossRef](#)]
6. He, W.W.; Liu, Y.; Tang, H.P.; Li, Y.P.; Liu, B.; Liang, X.P.; Xi, Z.P. Microstructural characteristics and densification behavior of high-Nb TiAl powder produced by plasma rotating electrode process. *Mater. Des.* **2017**, *132*, 275–282. [[CrossRef](#)]
7. Wu, Z.E.; Hu, R.; Zhang, T.B.; Zhou, H.; Li, J.S. Moisture induced environmental embrittlement of a high Nb containing TiAl alloy. *Mater. Sci. Eng. A* **2017**, *701*, 214–220. [[CrossRef](#)]
8. Djanarthany, S.; Viala, J.C.; Bouix, J. Development of SiC/TiAl composites: Processing and interfacial phenomena. *J. Mater. Sci. Eng. A* **2001**, *300*, 211–218. [[CrossRef](#)]
9. Liu, Y.X.; Wang, F.; Zhu, J.F.; Wang, X.F. Mechanical properties and microstructure of Al₂O₃/TiAl in situ composites doped with Cr₂O₃. *Mater. Sci. Eng. A* **2011**, *528*, 3337–3341.
10. Lapin, M.; Štamborská, T.; Pelachová, O. Fracture behaviour of cast in-situ TiAl matrix composite reinforced with carbide particles. *J. Mater. Sci. Eng. A* **2018**, *721*, 1–7. [[CrossRef](#)]
11. Rao, K.P.; Zhou, J.B. Characterization and mechanical properties of in situ synthesized Ti₅Si₃/TiAl composites. *Mater. Sci. Eng. A* **2003**, *356*, 208–218. [[CrossRef](#)]
12. Hu, D. Effect of boron addition on tensile ductility in lamellar TiAl alloys. *Intermetallics* **2002**, *10*, 851–858. [[CrossRef](#)]
13. Heredia, F.E.; He, M.Y.; Lucas, G.E.; Evans, A.G.; Deve, H.E.; Konitzer, D. The fracture resistance of directionally solidified dual-phase NiAl reinforced with refractory metals. *Acta Metall. Mater.* **1993**, *41*, 505–511. [[CrossRef](#)]
14. Krstic, V.D. On the fracture of brittle-matrix/ductile-particle composites. *Philos. Mag. A* **1983**, *48*, 695–708. [[CrossRef](#)]
15. Sun, X.; Yeomans, J.A. Ductile phase toughened brittle materials. *J. Mater. Sci. Technol.* **1996**, *12*, 124–134.
16. Yang, X.; Xi, Z.P.; Liu, Y.; Tang, H.P.; Hu, K.; Jia, W.P. Microstructure and fracture toughness of a TiAl–Nb composite consolidated by spark plasma sintering. *Trans. Nonferr. Met. Soc. China* **2012**, *22*, 2628–2632. [[CrossRef](#)]
17. Chen, Y.Y.; Niu, H.Z.; Kong, F.T.; Xiao, S.L. Microstructure and fracture toughness of a β phase containing TiAl alloy. *Intermetallics* **2011**, *19*, 1405–1410. [[CrossRef](#)]
18. Rao, K.T.V.; Odette, G.R.; Ritchie, R.O. Ductile-reinforcement toughening in γ -TiAl intermetallic-matrix composites: Effects on fracture toughness and fatigue-crack propagation resistance. *Acta Metall. Mater.* **1994**, *42*, 893–911.
19. Yoo, M.H.; Fu, C.L. Cleavage fracture of ordered intermetallic alloys. *Mater. Sci. Eng. A* **1992**, *153*, 470–478. [[CrossRef](#)]

20. Li, J.B.; Liu, Y.; Liu, B.; Wang, Y.; Zhao, K.; He, Y.H. Effect of Nb particles on the flow behavior of TiAl alloy. *Intermetallics* **2014**, *46*, 22–28. [[CrossRef](#)]
21. Sellars, C.M. *Proceedings of the International Conference on Mathematical Modelling of Hot Rolling of Steel*; Yue, S., Ed.; CIMM: Hamilton, ON, USA, 1990.
22. Wang, L.; Liu, Y.; Zhang, W.; Wang, H.; Li, Q. Optimization of pack parameters for hot deformation of TiAl alloys. *Intermetallics* **2011**, *19*, 68–74. [[CrossRef](#)]
23. Cao, R.; Lei, M.X.; Chen, J.H.; Zhang, J. Effects of loading rate on damage and fracture behavior of TiAl alloys. *Mater. Sci. Eng. A* **2007**, *465*, 183–193. [[CrossRef](#)]
24. Nicolas, B.; Frédéric, D.; Russell, G.; Andreas, M. Fracture of convoluted and lamellar $\alpha_2 + \gamma$ TiAl alloys. *Intermetallics* **2012**, *22*, 176–188.
25. Gupta, R.K.; Narayana Murtya, S.V.S.; Panta, B.; Agarwalab, V.J.Y.; Sinha, P.P. Constitutive modeling and processing map for elevated temperature flow behaviors of a powder metallurgy titanium aluminide alloy. *Mater. Sci. Eng. A* **2012**, *551*, 169–186. [[CrossRef](#)]
26. Kong, F.T.; Chen, Y.Y.; Zhang, D.L.; Zhang, S.Z. High temperature deformation behavior of Ti-46Al-2Cr-4Nb-0.2Y alloy. *Mater. Sci. Eng. A* **2012**, *539*, 107–114. [[CrossRef](#)]
27. Marketza, W.T.; Fischera, F.D.; Clemens, H. Deformation mechanisms in TiAl intermetallics—experiments and modeling. *Int. J. Plast.* **2003**, *19*, 281–321. [[CrossRef](#)]
28. Wang, Y.; Liu, Y.; Yang, G.Y.; Li, J.B.; Liu, B.; Wang, J.W.; Li, H.Z. Hot deformation behaviors of β phase containing Ti-43Al-4Nb-1.4W-based alloy. *Mater. Sci. Eng. A* **2013**, *577*, 210–217. [[CrossRef](#)]
29. Wang, Y.; Zhang, C.; Liu, Y.; Zhao, S.X.; Li, J.B. Microstructure characterization and mechanical properties of TiAl-based alloys prepared by mechanical milling and spark plasma sintering. *Mater. Charact.* **2017**, *128*, 75–84. [[CrossRef](#)]
30. Song, L.; Xu, X.J.; You, L.; Liang, Y.F.; Lin, J.P. Phase transformation and decomposition mechanisms of the $\beta_0(\omega)$ phase in cast high Nb containing TiAl alloy. *J. Alloys Compd.* **2014**, *616*, 483–491. [[CrossRef](#)]
31. Liu, B.; Liu, Y.; Li, Y.P.; Zhang, W.; Chiba, A. Thermomechanical characterization of β -stabilized Ti-45Al-7Nb-0.4W-0.15B alloy. *Intermetallics* **2011**, *19*, 1184–1190. [[CrossRef](#)]
32. Li, J.B.; Liu, Y.; Wang, Y.; Liu, B.; He, Y.H. Dynamic recrystallization behavior of an as-cast TiAl alloy during hot compression. *Mater. Charact.* **2014**, *97*, 169–177. [[CrossRef](#)]
33. Appel, F.; Paul, J.D.H.; Oehring, M. *Gamma Titanium Aluminide Alloys—Science and Technology*; Wiley VCH: Weinheim, Germany, 2011.
34. Makhutov, N.A.; Matvienko, Y.G. Griffith theory and development of fracture mechanics criteria. *Mater. Sci.* **1993**, *29*, 316–319. [[CrossRef](#)]
35. Zheng, Y.P.; Zeng, W.D.; Li, D.; Zhao, Q.Y.; Liang, X.B.; Zhang, J.W.; Ma, X. Fracture toughness of the bimodal size lamellar O phase microstructures in Ti-22Al-25Nb (at. %) orthorhombic alloy. *J. Alloys Compd.* **2017**, *709*, 511–518. [[CrossRef](#)]
36. Boehlert, C.J. The tensile behavior of Ti-Al-NbO + Bcc Orthorhombic alloys. *Metall. Mater. Trans. A* **2001**, *34*, 1977–1988. [[CrossRef](#)]

